remote sensing

MDPI

Article

NOx Emission Flux Measurements with Multiple Mobile-DOAS Instruments in Beijing

Yeyuan Huang [1,2], Ang Li [1,*], Pinhua Xie [1,2,3], Zhaokun Hu [1], Jin Xu [1], Xiaoyi Fang [4], Hongmei Ren [1,2], Xiaomei Li [1,2] and Bing Dang [5]

[1] Key Laboratory of Environmental Optics and Technology, Anhui Institute of Optics and Fine Mechanics, Hefei Institutes of Physical Science, Chinese Academy of Sciences, Hefei 230031, China; yyhuang@aiofm.ac.cn (Y.H.); phxie@aiofm.ac.cn (P.X.); zkhu@aiofm.ac.cn (Z.H.); jxu@aiofm.ac.cn (J.X.); hmren@aiofm.ac.cn (H.R.); xmli@aiofm.ac.cn (X.L.)

[2] School of Environmental Science and Optoeclectronic Technology, University of Science and Technology of China, Hefei 230026, China

[3] CAS Center for Excellence in Regional Atmospheric Environment, Institute of Urban Environment, Chinese Academy of Sciences, Xiamen 361000, China

[4] Chinese Academy of Meteorological Science, Beijing 100081, China; fangxy@cma.gov.cn

[5] Beijing Municipal Climate Center, Beijing 100089, China; dangbing@bj.cma.gov.cn

* Correspondence: angli@aiofm.ac.cn

Received: 2 June 2020; Accepted: 3 August 2020; Published: 6 August 2020

Abstract: NO_X ($NO_X = NO + NO_2$) emissions measurements in Beijing are of great significance because they can aid in understanding how NO_X pollution develops in mega-cities throughout China. However, NO_X emissions in mega-cities are difficult to measure due to changes in wind patterns and moving sources on roads during measurement. To obtain good spatial coverage on different ring roads in Beijing over a short amount of time, two mobile differential optical absorption spectroscopy (DOAS) instruments were used to measure NO_X emission flux from April 18th to 26th, 2018. In addition, a wind profile radar provided simultaneous wind field measurements for altitudes between 50 m and 1 km for each ring road measurement. We first determined NO_X emission flux of different ring roads using wind field averages from measured wind data. The results showed that the NO_X emission flux of Beijing's fifth ring road, which represented the urban part, varied from $(19.29 \pm 5.26) \times 10^{24}$ molec./s to $(36.46 \pm 12.86) \times 10^{24}$ molec./s. On April 20th, NO_X emission flux for the third ring was slightly higher than the fourth ring because the two ring roads were measured at different time periods. We then analyzed the NO_X emission flux error budget and error sensitivity. The main error source was the wind field uncertainty. For some measurements, the main emission flux error source was either wind speed uncertainty or wind direction uncertainty, but not both. As Beijing's NO_X emissions came from road vehicle exhaust, we found that emission flux error had a more diverse sensitivity to wind direction uncertainty, which improved our knowledge on this topic. The NO_X emission flux error sensitivity study indicated that more accurate measurements of the wind field are crucial for effective NO_X emission flux measurements in Chinese mega-cities. Obtaining actual time and high resolved wind measurements is an advantage for mega-cities' NO_X emission flux measurements. The emission flux errors caused by wind direction and wind speed uncertainties were clearly distinguished. Other sensitivity studies indicated that NO_X/NO_2 ratio uncertainty dominated flux errors when the NO_X/NO_2 ratio uncertainty was >0.4. Using two mobile-DOAS and wind profile radars to measure NOx emission flux improved the quality of the emission flux measuring results. This approach could be applied to many other mega-cities in China and in others countries.

Keywords: NO_X; emission flux; mobile-DOAS; mega-city

---

1. Introduction

Nitrogen oxides (NO_X, $NO_X = NO + NO_2$) is an important trace gas in the atmosphere [1]. It plays a key role in atmospheric chemical reactions and easily produces air pollution with excessive emissions [1,2]. China's rapid economic development in the 21st century has been accompanied by serious environmental pollution, especially air pollution [2–8]. Haze pollution events occur frequently in Jingjinji (Beijing, Tianjin, and Hebei province) due to the excessive emissions of NOx, sulfur dioxide (SO_2), and volatile organic compounds (VOCs) [9]. The project of the Jingjinji area air pollution control was launched in April 2017, led by the National Air Pollution Prevention and Control Association, China (NAPCA). Several research efforts have been dedicated to the study of pollution causes and control measures to prevent air pollution events [6–10]. According to the campus of Peking University, the nitrate formation of $PM_{2.5}$ was evident in the haze pollution of Jingjinji in 2014. The ratio of nitrates in $PM_{2.5}$ in Jingjinji obviously increased because of sulphate emission reduction [9]. NO_X is now a major source of inorganic pollutants in the Jingjinji area.

Urbanization has significantly increased NO_X emissions from vehicles in Chinese mega-cities. Beijing, a typical mega-city in China, has no factories in its downtown area, except for a power plant near the east side of the fifth ring. The power plant emits little NO_X due to the region's strict gas pollution control policies. Hence, most of the NO_X emissions can be attributed to road vehicles. Figure 1 presents annual NO_X emissions of vehicle emissions and the ratio of vehicle NO_X emissions compared to the total NO_X emissions in Beijing from 2011 to 2017. Due to the implementation of traffic control policies, the NO_X emission flux emitted by vehicles decreased from 2011 to 2014 and from 2015 to 2016. However, the NO_X emissions from vehicles are increasing year by year (nearly 85% in 2017). This happens in other mega-cities such as Shanghai and Guangzhou. Studying the mega-cities' NO_X emissions from vehicles has great significance for air pollution control.

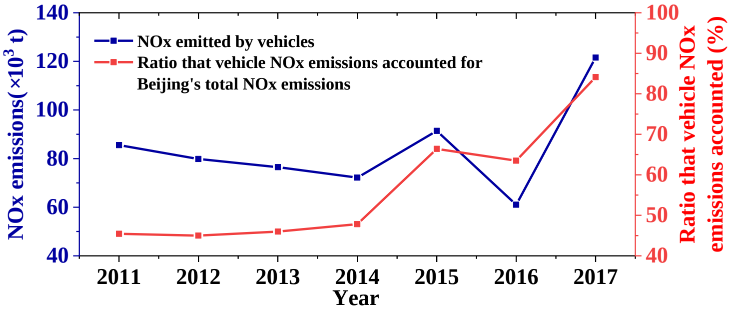

Figure 1. The annual NO_X emissions of vehicles in Beijing from 2011 to 2017 and the percentage of vehicles emitting NOx over total NOx emissions in Beijing. (NO_X emission data source: Beijing Municipal Ecological Environment Bureau).

Differential optical absorption spectroscopy (DOAS) is a remote sensing technique developed in the 1970s and used for measuring atmospheric gases [11,12]. The DOAS technique is widely applied to measure trace gases [13–15]. An important application of the DOAS method is to measure the gas emission flux, such as NOx and SO_2, using the close integral method (for area emitters) and the flow rate method (for point sources) [16,17]. Mobile-DOAS uses sunlight as its light source and places a DOAS instrument on a mobile platform, which is a technological improvement for the technique. This platform can be a car or an airplane [18–22]; here, we focus on cars. Mobile-DOAS has been widely used for emission flux measurements and has achieved good results [23–32]. Previous studies have aimed at point sources [25,26] or area emitting [27–32] measurements taken from stationary emission sources. Some studies have also used mobile-DOAS to examine CHIMERE chemistry transport model (CTM) outputs or emission inventories [26,31]. Improvements in the mobile-DOAS measurements quality has been highly requested by the scientific community to enhance the capabilities needed to determine NOx emission fluxes particularly in Chinese mega-cities.

Road vehicles, which are moving sources, are now the main emission sources of NO_X in Chinese mega-cities. The large spatial scales of these cities and the predominance of moving sources make NO_X emission flux measurements rather complicated for mobile-DOAS. The large spatial scale of these cities leads to two issues: unknown details of NO_X emission fluxes in inner cities and the large amount of time needed to take necessary measurements. This directly relates NO_X emission flux measurements needed for the high-quality wind field. Moving sources have also introduced a problem: the spatial tropospheric NO_2 vertical column density (VCD) distributed along the measurement route has a strong relationship not only to wind field dispersion but also to traffic flow and traffic jams. This indicates that high value VCDs can appear anywhere along roads and that the NO_X flux error budget and sensitivity to the wind field might have unexpected differences.

This paper is organized as follows: Section 2 describes the experiments, instruments, and algorithms. In Section 3, the measurement results are presented. Section 4 concentrates on the discussion. In Section 5, the conclusions are presented.

2. Experiment and Methodology

2.1. Experiment Overview

For area emission flux measurements using mobile-DOAS, the close integral method is usually used [30]. Therefore, the ring structure of Beijing is ideal for the mobile-DOAS emission estimations. We chose 4 ring roads (the second ring, third ring, fourth ring, and fifth ring) for these measurements. The mean distance *r* from the measurement location to the city center was about 4.5 km, 7 km, 10 km, and 15 km for the second ring, third ring, fourth ring, and fifth ring, respectively. Two sets of the same mobile-DOAS model and wind profile radar were selected to perform cooperative measurements. We used DOAS1 and DOAS2 to mark the 2 mobile-DOAS sets. DOAS1 was used to measure the third and fourth ring, and the rest were measured by DOAS2. The wind profile radar provided simultaneous measurements of the wind field. Figure 2 shows the measurements routes and wind profile radar measurement location.

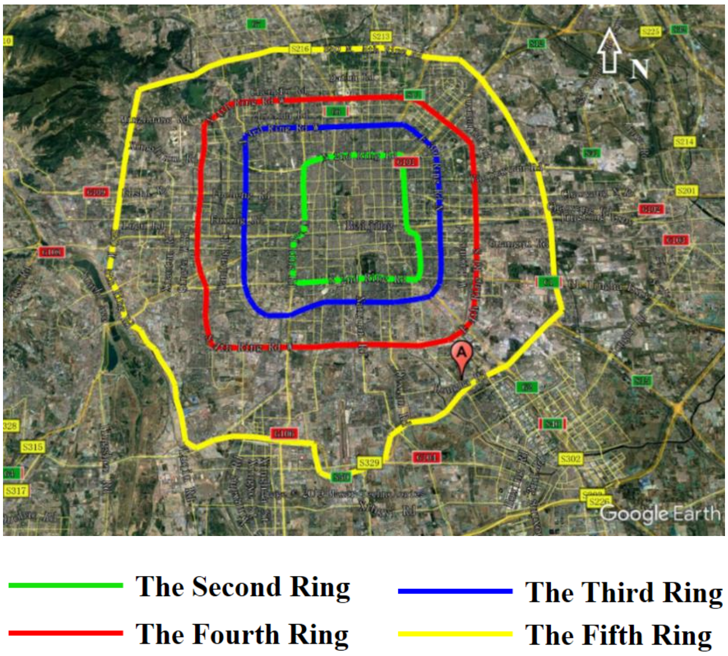

Figure 2. The ring roads of Beijing, China. Map data © Google Earth (point A is the location of the wind profile radar).

2.2. Mobile-DOAS

2.2.1. Mobile-DOAS Instrument

There are two types of mobile-DOAS instruments: one working in the zenith sky configuration [18] and the other in the multi axis (MAX) configuration [17]. The instruments for our experiment were carefully chosen, as there are many tall buildings in Beijing that can directly act on the sunlight scattering or reflection. The air mass factor (AMF) is also a problem, as it cannot be accurately estimated. Therefore, the application of mobile MAX-DOAS in our experiment is limited. We chose the mobile zenith-sky DOAS and, for simplicity, used the “mobile-DOAS” abbreviation.

The mobile-DOAS consists of several parts. A telescope, placed on the top of the mobile, is used to collect the scattering sunlight from the zenith sky. A spectrometer with a 0.5 nm resolution and a 290–438 nm of spectral range is located inside the temperature stabilization system placed within the car. An optical fiber is used to transmit the sunlight from the telescope to the spectrometer. The other parts include the GPS module used to record the car’s moving trail and a computer to collect the data. The mobile-DOAS system and its measurements principle are outlined in Figure 3.

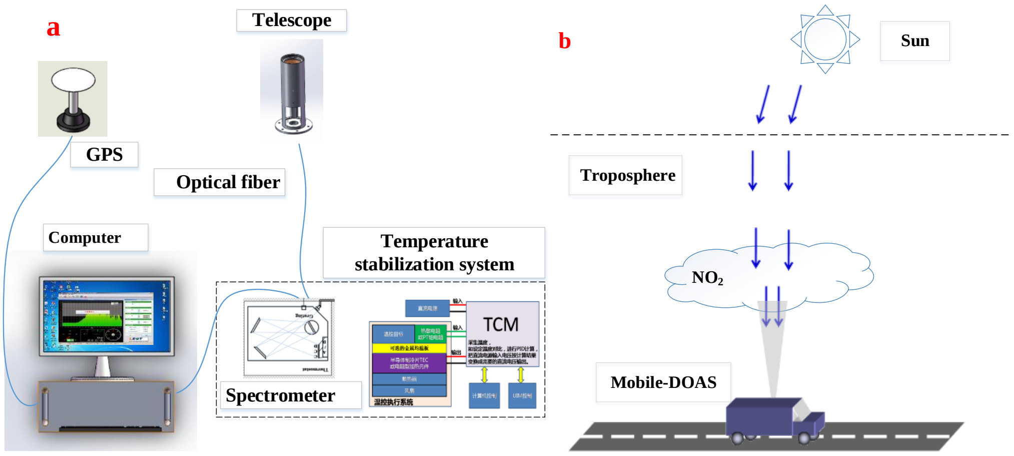

Figure 3. (**a**) The mobile zenith-sky differential optical absorption spectroscopy (DOAS) system; (**b**) the measurement principle of the mobile-DOAS system.

2.2.2. Retrieval Algorithm

In this study, we used the QDOAS software (version 3.2, 2017) to retrieve the tropospheric NO_2 differential slant column density (DSCD) from the measured spectra [33]. All the measured spectra were divided by a Fraunhofer reference spectrum, which was relatively “clean”, and the ring was calculate by DOASIS [34,35]. The absorption cross-sections used in the QDOAS for the 2 mobile-DOAS and fitting window are listed in Table 1. Figure 4 shows a DOAS fitting example for NO_2 and the fitting residual.

Table 1. NO_2 slant column density (SCD) retrieval fit setting.

Fitting Parameter	NO_2
Fitting windows	(338~370) nm
Polynomial order	5
NO_2	Vandaele, 1996 (220K, 298k)
O_3	Bogumil, 2003 (223K, 243K)
O_4	Thalman, 2013 (293K)
HCHO	Meller, 2000 (297K)
Ring	by DOASIS

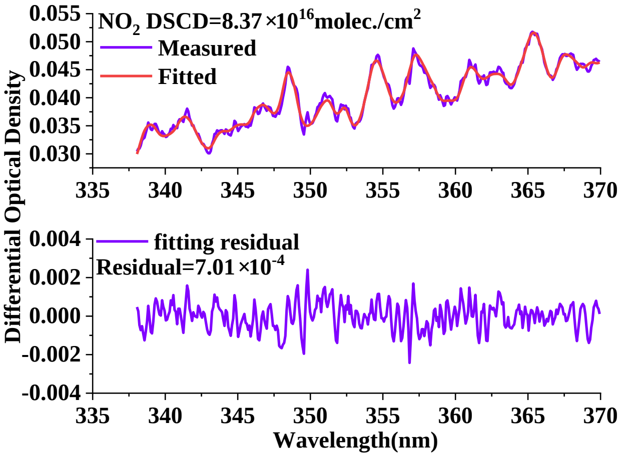

Figure 4. (Upper plot) DOAS fitting example for NO_2; (bottom plot) fitting residual.

The tropospheric NO_2 VCD taking part in the NO_X emission flux calculations is obtained from NO_2 DSCD divided for the AMF according to the following formula [17]:

$$VCD = \frac{DSCD_{trop} - DSCD_{offset}(t_i)}{AMF_{trop}} \quad (1)$$

where $DSCD_{trop}$ denotes the tropospheric NO_2 DSCD and AMF_{trop} is the tropospheric AMF.

$DSCDoffset(t_i)$ is the difference of the reference SCD and stratospheric SCD, and is a smooth function of time [17]. $DSCDoffset(t_i)$ depends on the solar zenith angle (SZA), where the dependence is weak when SZA <80° [17]. The SZA during the measurements was <55°. Therefore, the $DSCDoffset(t_i)$ was negligible in our measurements.

AMF_{trop} can be computed with a radiation transfer model simulation or with geometric approximations [36]. In this study, we performed the Monte Carlo radiative transfer model [37] simulations to determine AMF_{trop}. The AMF_{trop} was simulated under different SZA and different aerosol scenarios. The mean NO_2 load from national environment observation stations (Dongsi station, Aoti Station, Gucheng station and Wanliu station) in Beijing was about 43 ppb. AMF simulation results indicated that the AMF_{trop} was typically between 1.05 and 1.4. The higher SZA and higher aerosol, the larger the AMF_{trop}. Since SZA was less than 45° for most of the measurement time ($AMF_{trop} < 1.3$), we applied a typical AMF_{trop} value of 1.15 with an error of ±0.1.

2.2.3. Retrieval Comparison

We used 2 mobile-DOAS systems to measure the NO_X emission flux for the first time. To ensure measurement quality, two retrieval comparisons were performed.

The first tested the retrieval homogeneity of the 2 mobile-DOAS systems. On 14 April 2018, we placed 2 DOAS instruments on 1 mobile to measure the NO_2 of an industrial park located in Handan, Hebei province. The 2 DOAS apparatus' time resolutions were set as 10 s and measured NO_2 almost simultaneously. The comparison results of NO_2 VCDs apparatuses are shown in Figure 5a and the correlation coefficient (R^2) of the 2 sets was found to be 0.976. The high retrieval homogeneity shows the efficacy of cooperatively measuring the area emission flux using the 2 DOAS sets.

The second was to ensure mobile-DOAS instrument performance. The retrieval homogeneity was ensured, so we only needed to compare one of the mobile-DOAS (DOAS1) instruments with another instrument. A ground-based MAX-DOAS located on the roof of the Beijing south observation station building (116.468° N, 39.798° E) was selected as the reference instrument. The mobile-DOAS and MAX-DOAS systems were put together to measure NO_2 on April 16th. The 2 apparatuses time resolutions were 10 s and measured NO_2 almost simultaneously. Figure 5b presents the comparison result, which shows good agreement with a correlation coefficient (R^2) of 0.932.

These two comparison results demonstrated that the 2 mobile-DOAS systems can perform a good quality measurement.

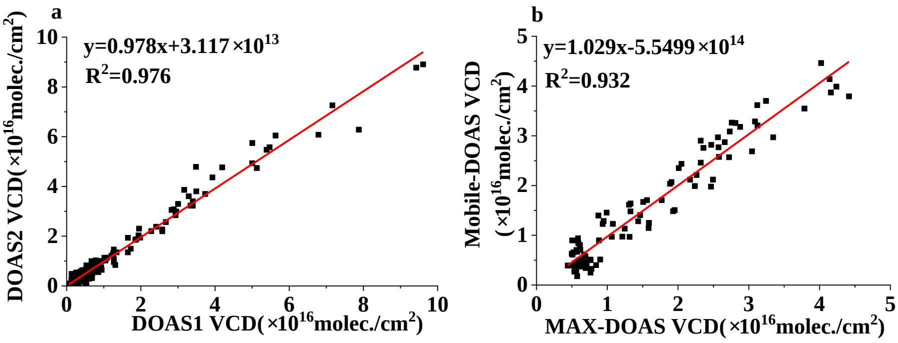

Figure 5. Retrieval comparison results. (**a**) The retrieval homogeneity of the 2 mobile-DOAS instruments with a correlation coefficient (R^2) of 0.976; (**b**) the comparison result for mobile-DOAS (DOAS1) and MAX-DOAS with a correlation coefficient (R^2) of 0.932.

2.3. *Wind Field Measurement and Average Wind Field*

2.3.1. Wind Profile Radar

The wind field uncertainty is the main error source of mobile-DOAS emission flux measurements [27]. Several studies on mobile-DOAS indicate that having a wind profile is crucial for mobile-DOAS [18,22,24,26,31]. A near real-time measurement of the wind field is recommended for calculating the emission flux [18,26,31]. To enable an accurate emission flux measurement, we chose a wind profile radar to obtain wind profile data.

Wind field measurements involve two possible methods. The first uses a mobile wind profile radar with a mobile-DOAS to measure the wind field. The second uses stationary observation. Wind profile radar vehicles are usually large and inconvenient to enter/exit the second and third ring in Beijing because of the strict restriction policies on vehicles. Therefore, we measured the wind field data using stationary observations. An advantage of this approach is that the 2 DOAS sets only need 1 shared wind profile radar to obtain the wind profile data. Furthermore, the wind field and wind field uncertainty for each ring road measurement could be determined.

The tall buildings in downtown Beijing markedly affected the wind field, so wind field observation sites could not be selected randomly. The comprehensive meteorological experimental observation station (116.466° N, 39.796° E) was used for Beijing's meteorological research so we chose this station to measure the wind field data. The location of the station is shown in Figure 2 marked with point A.

A radar for boundary wind profiling placed in a square cabin was also used in this experiment. The wind profile radar can measure the wind profile under a height of 5 km, with a height resolution of 50 m and a time resolution of 2 min. Since a wind profile under 1 km met our needs [31], we only measured the wind profile under a height of 1 km.

2.3.2. Wind Field Statistics

The wind parameters taking part in the NO_X emission flux calculations are for average wind speed and wind direction, while the data furnished by the wind profile radar measured the time series of wind profiles. In order to calculate NO_X emission flux, we developed 2 methods for averaging wind field profiles. The first used vector-based statistics and the second used scalar-based statistics. Both presented the same behavior and were equivalent [38]. Here, we chose scalar-based statistics.

Wind data were measured as a time series wind profile and averaging was be implemented in 2 steps. The first step averaged each height of the wind field for each time series to generate a time averaged wind profile, while the second step averaged the time averaged wind profile by using the exponential-weight method.

1. Wind field time averaging

First, we calculated the time averaged wind speed. The average wind speed and its uncertainty were determined by Equations (2) and (3), respectively.

$$\overline{w(z_j)}_t = \frac{1}{N}\sum_{i=1}^{N} w(z_{ji}) \tag{2}$$

$$\sigma(w_{zj})_t = \sqrt{\frac{1}{N-1}\sum_{i=1}^{N}\left[w(z_{ji}) - \overline{w(z_j)}_t\right]^2} \tag{3}$$

where i is the data measured at time i, z_j is the height, and j is the layer series. The subscript t represents the average.

We then averaged the wind direction. Wind direction distribution is subject to wrapped normal distribution, so we introduced wrapped normal distribution to determine the average wind direction and its uncertainty [38–40]. The wrapped normal distribution probability density is given with:

$$f(\mu|\theta,\sigma) = \frac{1}{\sqrt{2\pi}\sigma}\sum_{\kappa=1}^{\infty} exp\left[\frac{-(\theta-\mu+2\pi\kappa)^2}{2\sigma^2}\right],\ 0 \le \theta \le 2\pi \tag{4}$$

where θ is the wind direction, μ is the expectation, and σ is the standard deviation. Since the wind direction is between 0 and 2π, we let κ equal 0. The wind direction uncertainty of the measured wind data is

$$\sigma(\theta_{zj})_t = \sqrt{ln(\rho_{zj}^2)} \tag{5}$$

where $\rho_{zj}^2 = (\overline{cos\theta}_{zj})^2 + (\overline{sin\theta}_{zj})^2$, $\overline{cos\theta}_{zj} = \frac{1}{N}\sum_{i=1}^{N} cos\theta_{zji}$, $\overline{cos\theta}_{zj} = \frac{1}{N}\sum_{i=1}^{N} sin\theta_{zji}$.

The average wind direction is

$$\overline{\theta > (z_j >)}_t = \begin{cases} arctan\left(\frac{\overline{sin\theta_{zj}}}{\overline{cos\theta_{zj}}}\right), \overline{cos\theta}_{zj} > 0 \\ arctan\left(\frac{\overline{sin\theta_{zj}}}{\overline{cos\theta_{zj}}}\right) + \pi, \overline{cos\theta}_{zj} < 0 \end{cases} \tag{6}$$

In this step, the wind speed uncertainty σ_{wt} and the wind direction uncertainty $\sigma_{\theta t}$ introduced by time averaging were determined by Equation (7) according to the error combination law, which are:

$$\sigma_{wt} = \sqrt{\sum_{j=1}^{M}\left[Q_{zj}\cdot\sigma(w_{zj})_t\right]^2},\ \sigma_{\theta t} = \sqrt{\sum_{j=1}^{M}\left[Q_{zj}\cdot\sigma(\theta_{zj})_t\right]^2} \tag{7}$$

where Q_{zj} is the weight function determined by Equation (8).

2. Wind profile averaging

After the time averaging, the next step was to average the wind field by the NO_X concentration's exponentially decreasing profiles. This was an exponential weight function [29,31] and the weight at the height of z_j is:

$$Q_{zj} = \frac{exp(-z_j/z_0)}{\sum_{j=1}^{M} exp(-z_j/z_0)} \tag{8}$$

Then, the final average wind speed $\overline{w}_z$ and the average wind direction $\overline{\theta}_z$ are given with:

$$\overline{w}_z = \sum_{j=1}^{M}\left[Q_{zj}\cdot\overline{w(z_j)}_t\right],\ \overline{\theta}_z = \sum_{j=1}^{M}\left[Q_{zj}\cdot\overline{\theta(z_j)}_t\right] \tag{9}$$

where z_0 is the scale height, which is assumed to be 500 m in summer and 300 m in winter [31]. In spring and autumn, z_0 was chosen as the average of the winter and summer seasons, i.e., 400 m. The z_0 we chose is a rough estimate and has a rather small influence on the average wind field [31].

In this step, the uncertainty caused by the wind profile was introduced. According to statistical theory, the wind speed σ_{wz} and the directional uncertainty $\sigma_{\theta z}$ of the wind profile is:

$$\sigma_{wz} = \sqrt{\sum_{j=1}^{M}\left[Q_j\left(\overline{w}_z-\overline{w(z_j)}_t\right)\right]^2},\ \sigma_{\theta z} = \sqrt{\sum_{j=1}^{M}\left[Q_j\left(\overline{\theta}_z-\overline{\theta(z_j)}_t\right)\right]^2} \tag{10}$$

Therefore, the total uncertainty of the wind speed σ_w and the wind direction σ_θ are:

$$\sigma_w = \sqrt{\sigma_{wz}^2+\sigma_{wt}^2},\ \sigma_\theta = \sqrt{\sigma_{\theta z}^2+\sigma_{\theta t}^2} \tag{11}$$

2.4. Determination of the NO_X Emission Flux

There are two steps to determine the NO_X emission flux.

The first step is to determine the NO_2 emission flux using the closed integral method is given as

$$F_{NO2} = \oint VCD\ \vec{w}\ \vec{n}\ ds \tag{12}$$

where VCD is the NO_2 VCD, $\vec{w}$ is the wind filed, and $\vec{n}$ is the unit vector orthogonal to the car's moving direction. The discrete form of Equation (12) is given with [25]

$$F_{NO2} = \sum_i \left[VCD_i \cdot w \cdot (cos\theta \cdot s_{iy} - sin\theta \cdot s_{ix})\right] \tag{13}$$

where w is the average wind speed and θ is the average direction. $\vec{s_i} = (s_{ix}, s_{iy})$ is the car's movement vector. VCD_i is the tropospheric NO_2 VCD retrieved from the spectra measured by mobile-DOAS.

Then, we determined the NO_X emission flux with NO_X/NO_2 ratio correction and NO_X lifetime correction [29].

$$F_{NOx} = R_{NOx} \cdot c_\tau \cdot F_{NO2} \tag{14}$$

where R_{NOx} is the mean NO_X/NO_2 ratio. R_{NOx} is sensitive to meteorological conditions, other trace gases, and emission sources [32]. However, for Beijing, the R_{NOx} was highly sensitive to emission sources because many vehicles on the road give off NO and consume a large amount of O_3. This may result in significant O_3 consumption, which will in turn lead to a higher NO_X/NO_2 ratio near the surface. Therefore, the R_{NOx} observed on the ground should be carefully used. An understanding of the mean R_{NOx} value at different heights is thus important. An available method is to derive the mean R_{NOx} from the European Center for Medium-Range Weather Forecasts (ECMWF) CAMS model with the NO_2 and NO products under different heights. The mean R_{NOx} derived from different heights is used in this study at a height under 1 km at a UTC time of 6:00 (LT 14:00).

$c_\tau = exp\left(\frac{r}{w \cdot \tau}\right)$ is the NO_X atmospheric lifetime decay correction factor, r is the mean distance from the measurement center to the measurement location, and we have provided these data in Section 2.1. τ is the NO_X mean lifetime in atmosphere. In urban areas it varies from 3 h to 12 h in different seasons [31]. Usually, the NOx lifetime correction is sensitive to the lifetime when the wind speed is very low (<1 m/s) in mega-city measurements because NO_X decay is a lifetime exponential function. However, accurate lifetime correction is not very sensitive when the wind speed is larger than 1 m/s. In this study, average wind speeds are all above 1.5m/s. Therefore, we roughly assumed the urban NO_X mean lifetime to be about 5 h in spring [29]. It should also be noted that Equation (14) is for NO_X lifetime correction of total NO_X emissions. As Beijing has strong NO_X emissions within fourth and fifth ring roads, NO_X influx and outflux [24] lifetime correction for the flux of fourth and fifth ring roads are not so evident. There is a 5%~11% difference between the correction for total flux correction and correction for influx and outflux. The lifetime correction for NO_X influx and outflux is important when there is little difference between influx and outflux [31]. Differences between NO_X influx and outflux for second and third ring roads are relatively small so that lifetime correction for influx and outflux is important. However, the spatial scales of second and third ring roads are rather small. Lifetime correction for NO_X influx and outflux have little influence from the correction for total NO_X emissions. As a result, we applied lifetime correction for the NO_X influx and outflux of fourth and fifth ring roads.

3. Results

3.1. Average Wind Field

Using the statistical method outlined in Section 2.2.2, we first calculated the time averaged wind field to generate corresponding wind profile. Then, we averaged the time averaged wind profile. The average wind field and its uncertainty for different ring roads are listed in Table 2. The average wind field in Table 2 was used to determine the NO_X emission flux in Section 4.

Table 2. The ring roads' measuring data, measuring time, averaged wind field, and its uncertainty on April 18th, 20th, 24th, 25th, and 26th, 2018.

Date (2018)	Ring Roads and Measuring Time (Beijing Time)	Averaged Wind Speed and Its Uncertainty (m/s)	Averaged Wind Direction and Its Uncertainty (°)
April 18th	The second ring (12:40~13:27)	2.325 ± 0.643	55.644 ± 17.039
	The third ring (12:03~13:11)	2.285 ± 0.638	65.176 ± 13.735
	The fourth ring (9:39~11:24)	1.738 ± 0.501	70.651 ± 17.302
	The fifth ring (9:27~11:56)	1.736 ± 0.494	67.317 ± 15.497
April 20th	The second ring (13:18~14:32)	2.905 ± 0.779	68.607 ± 15.859
	The third ring (12:01~13:21)	3.553 ± 0.959	64.944 ± 13.220
	The fourth ring (9:33~11:21)	3.423 ± 0.919	61.889 ± 20.926
	The fifth ring (9:24~12:22)	3.501 ± 0.942	60.662 ± 15.265
April 24th	The second ring (11:24~12:15)	2.183 ± 0.551	255.665 ± 13.897
	The third ring (9:56~11:03)	2.721 ± 0.704	260.323 ± 20.409
	The fourth ring (11:09~12:47)	1.973 ± 0.512	255.457 ± 13.760
	The fifth ring (9:41~11:03)	2.83 ± 0.737	260.666 ± 21.051
April 25th	The second ring (13:19~14:07)	2.826 ± 0.730	44.126 ± 8.448
	The third ring (12:28~13:36)	2.621 ± 0.676	43.218 ± 9.216
	The fourth ring (11:03~12:26)	1.956 ± 0.545	41.982 ± 21.501
	The fifth ring (9:58~12:28)	2.14 ± 0.582	45.945 ± 19.045
April 26th	The second ring (12:08~13:30)	1.912 ± 0.506	273.92 ± 17.226
	The third ring (11:36~13:10)	1.537 ± 0.413	276.556 ± 15.009
	The fourth ring (9:42~11:32)	1.686 ± 0.459	255.23 ± 14.349
	The fifth ring (9:33~11:53)	1.571 ± 0.431	254.648 ± 14.211

3.2. Determination of NO_2 VCD

We used Equation (1) to calculate tropospheric NO_2 VCDs. After determining the NO_2 VCDs, we plotted the overall NO_2 VCDs with the GPS data shown in Figure 6. From the results, NO_2 VCDs varied from 1.38×10^{15} molec./cm^2 to 8.0×10^{16} molec./cm^2. As we mentioned in Section 1, the NO_2 VCD has a strong relationship with traffic flow and traffic jam, so high NO_2 VCD distribution along measurement routes had no obvious pattern. This strongly impacted the emission flux error estimation, which we discuss in Section 4.3.

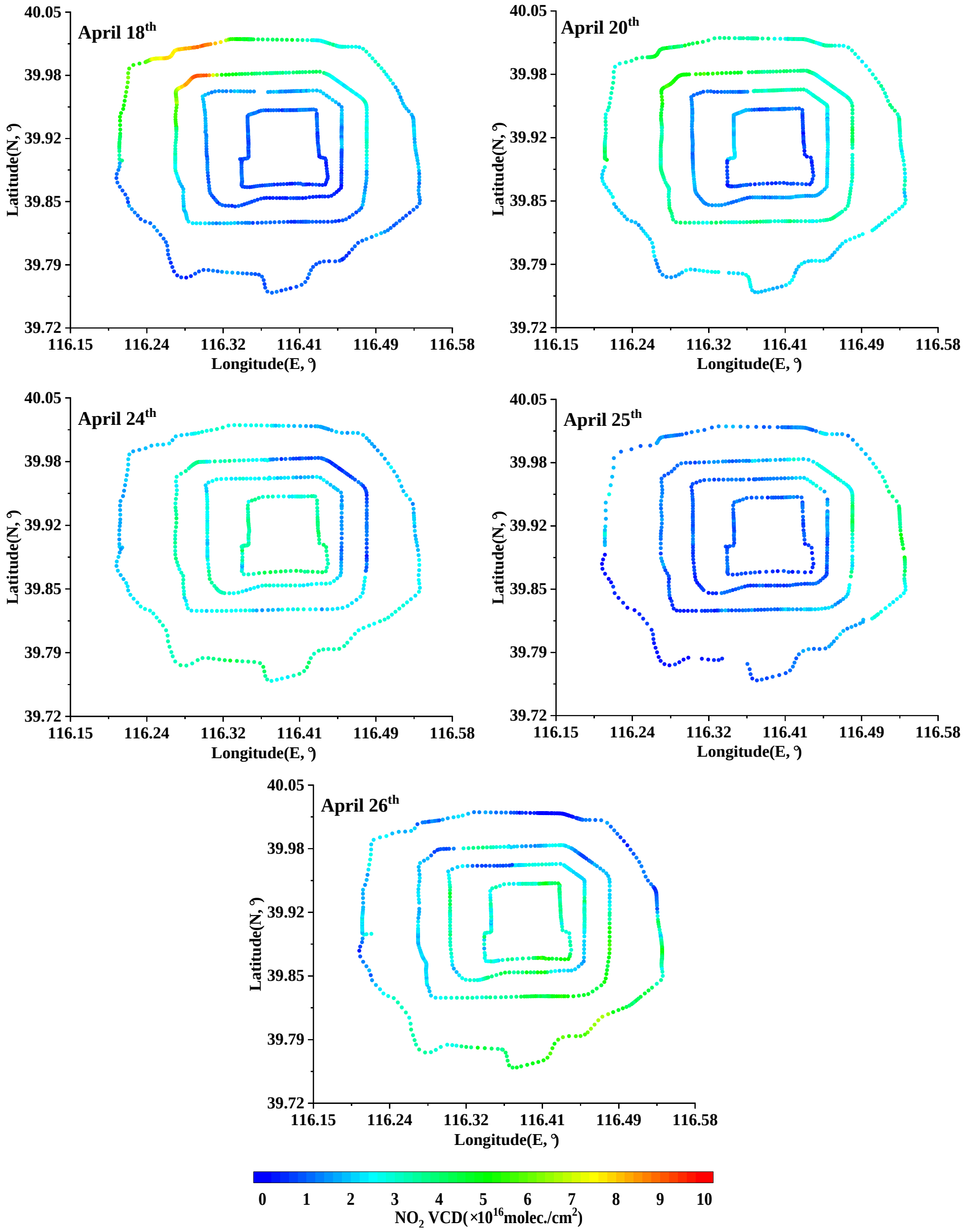

Figure 6. NO_2 VCD distribution of Beijing's ring roads on April 18th, 20th, 24th, 25th, and 26th. From outside to inside, the ring roads are the fifth ring, fourth ring, third ring, and second ring.

3.3. Comparison of TROPOMI and Mobile-DOAS VCDs

In this study, mobile-DOAS NO_2 VCDs were compared with a Tropospheric Monitoring Instrument (TROPOMI) to measure tropospheric NO_2 VCDs over Beijing. For places without significant emission sources, ground-based observations can compare with satellite products within 2 h around the satellite's overpass time [9]. As there are many moving sources in Beijing, we used mobile-DOAS tropospheric NO_2 VCDs within 1 h around the overpass time for comparison. Figure 7a–e presents the spatial distribution of mobile-DOAS and satellite tropospheric NO_2 VCDs over Beijing. The two datasets generally agree with each other, yet for some observations the satellites underestimated NO_2 VCDs compared with mobile-DOAS (subfigures (b) and (e)). The tropospheric NO_2 VCD daily average for the mobile-DOAS and TROPOMI correlation coefficient (R^2) was 0.7, showing a relatively good agreement, as shown in subfigure (f).

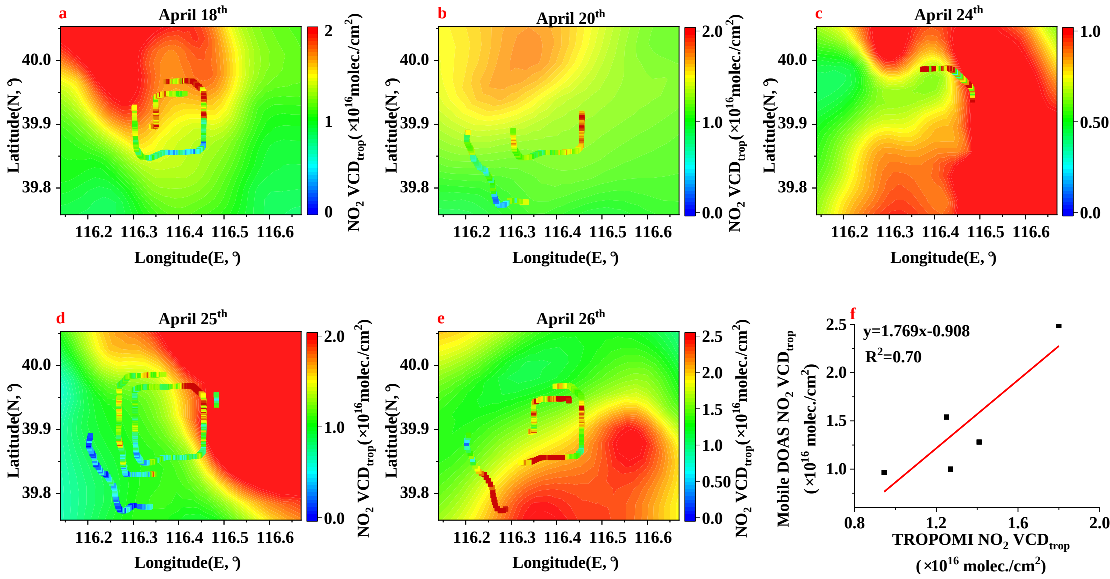

Figure 7. (**a**–**e**) are the mobile-DOAS and satellite tropospheric NO_2 VCD spatial distribution; (**f**) is the correlation coefficient (R^2).

4. Discussion

4.1. NO_X Emission Flux Error Sources

NO_X emission flux errors mainly come from the VCD, wind speed, wind direction, car moving vector, NO_X/NO_2 ratio, and lifetime measurement errors or uncertainty [27–32]. The NO_X emission flux is obtained with:

$$\Delta F_{NOx} = \sqrt{\Delta F_{RNOx}^2 + \Delta F_{c\tau}^2 + \Delta F_{VCD}^2 + \Delta F_s^2 + \Delta F_\theta^2 + \Delta F_w^2} \tag{15}$$

where ΔF_{RNOx} represents the NO_X flux error introduced by the NO_X/NO_2 ratio uncertainty. The NO_X/NO_2 ratio uncertainty we assumed to be about ± 0.1.

$\Delta F_{c\tau}$ is the NO_X flux error introduced by the NO_X atmospheric lifetime uncertainty. The NO_X atmospheric lifetime uncertainty we assumed here to be about ±1 h. It should be noted that the NO_X lifetime uncertainty estimation in this study was rough and had a small influence on the error budget (see Section 4.3).

ΔF_{VCD} is the NO_X emission flux error introduced by NO_2 VCD error. Because $VCD = DSCD_{trop}/AMF_{trop}$, the VCD error is determined by DSCD retrieval error and AMF_{trop} uncertainty. The NO_2 DSCD is retrieved by the QDOAS software so that DSCD error can be mainly attributed to the DOAS retrieval error. The AMF error that we simulated was approximately ±0.1.

ΔF_s is the NO_X emission flux error caused by the car movement vector measurement error. The car movement vector was recorded by GPS and the GPS error was <1.5 m.

ΔF_w and ΔF_θ represent the emission flux error caused the wind speed uncertainty and wind direction uncertainty, respectively. The wind speed uncertainty and wind direction uncertainty are mainly attributed to the wind fluctuation in space and time during the measurements. The uncertainties are listed in Table 2.

4.2. NO_X Emission Flux and Error

One of the motivations of this work was to obtain good spatial coverage of mega-cities' NO_X emission flux in a short amount of time. The NO_X emission flux values of different ring roads obtained using our measurements can provide useful and detailed information on road vehicle exhaust in Beijing. The NO_X emission flux and the errors results are shown in Figure 8.

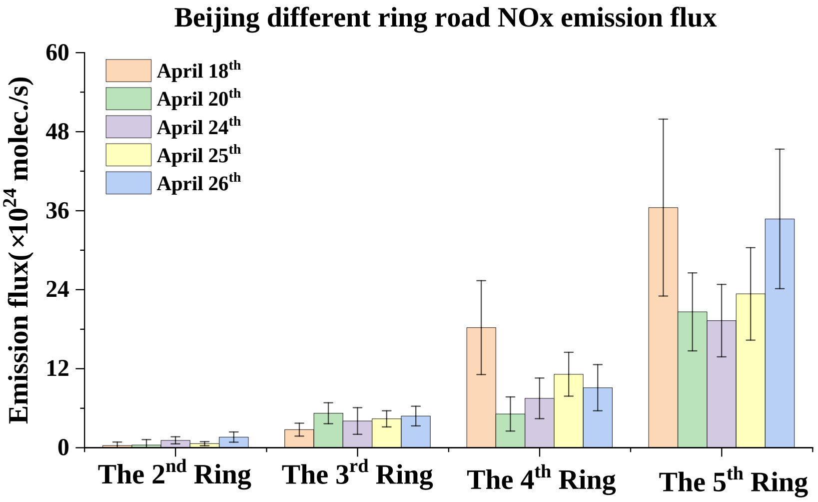

Figure 8. The NO_X emission flux and its error for the ring roads in Beijing; measurements taken on April 18th, 20th, 24th, 25th, and 26th, 2018.

During the measurement, the NO_X emission flux of the second ring varied from $(0.30 \pm 0.51) \times 10^{24}$ molec./s to $(1.53 \pm 0.75) \times 10^{24}$ molec./s; the third ring varied from $(2.60 \pm 0.95) \times 10^{24}$ molec./s to $(5.21 \pm 1.42) \times 10^{24}$ molec./s; the fourth ring varied from $(5.01 \pm 3.43) \times 10^{24}$ molec./s to $(18.22 \pm 6.82) \times 10^{24}$ molec./s; and the fifth ring, representing downtown Beijing, varied from $(19.29 \pm 5.26) \times 10^{24}$ molec./s to $(36.46 \pm 12.86) \times 10^{24}$ molec./s. The fifth ring's NOx emission flux mean value was about 26.89×10^{24} molec./s, which was ~13.08% higher compared to the estimations by Li et al. in November, 2014, under a low wind speed (<3 m/s) [41]. Significant improvement of NO_X emissions within the fifth ring was not found in this study, although a strict traffic control policy has been implemented in Beijing for these years.

The NOx emission flux showed an overall increase from the second ring to the fifth ring. This indicates that little NO_X was emitted from other sources within the fifth ring (mainly the road vehicles emissions). Because the traffic conditions vary day to day, the NO_X emission flux of different ring roads also vary day to day, which can be easily found in our measurements. For example, the fifth ring's NO_X emission flux was 36.46×10^{24} molec./cm^2 on April 18th and 34.740×10^{24} molec./cm^2 on April 26th, while it was 20.63×10^{24} molec./cm^2 on April 20th, 19.29×10^{24} molec./cm^2 on April 24th, and 23.35×10^{24} molec./cm^2 on April 25th. Other ring roads that were measured on different dates also show this characteristic. This analysis reveals that the large amount NO_X emissions from road vehicles may create additional challenges for the accurate measurements of NO_X emissions in the mega-cities of China.

Some interesting findings from our results were the NO_X emission flux differences between the third and fourth ring. On April 18th, the NO_X emission flux values of the third and fourth ring were 2.74×10^{24} molec./cm^2 and 13.01×10^{24} molec./cm^2, respectively. It seemed reasonable that for the fourth ring road's NO_X emissions would be higher than those of the third ring. However, on April 20th, the NO_X emission flux values of the third and fourth ring were 5.22×10^{24} molec./cm^2 and 5.10×10^{24} molec./cm^2, respectively. The fourth ring's NO_X emissions were slightly lower than the third ring's on April 20th. The differences in the NO_X emission flux values can be attributed to the number of road vehicles. The direct reason for the different number of road vehicles was the different measurement time periods. A potential issue was that there may be an indirect cause behind the differences in the number of road vehicles. The number of road vehicles during different time periods was decided by factors such as the citizen's workplace, the office area aggregation scale in the city, and the business style. Therefore, detailed NO_X emission flux studies in mega-cities can provide important information for urbanization in China.

4.3. Error Budget and Sensitivity

4.3.1. Error Budget

Studying the emission flux error budget and sensitivity can improve our knowledge about the area emitters' flux measurements, especially in mega-cities. Therefore, another motivation of this work was to study the error budget of NO_X emission flux measurements in mega-cities and to determine the emission flux sensitivity factors in detail. We chose the 18th and 20th measurement results as typical examples to analyze.

The tropospheric NO_2 VCD spatial distribution has a strong relationship to traffic flow and traffic jams. This suggests that NO_X emission flux error may be very sensitive to wind field uncertainty.

Because the emission flux error is propagated and combined (and is not linear), using percentage indicator is not a good way to evaluate the error budget. We thus used R_i^2 as the indicator:

$$R_i^2 = \frac{\Delta F_i^2}{\Delta F_{NOx}^2} \tag{16}$$

where ΔF_i is the emission flux error and i represents the error source. Because $\sum R_i^2 = 1$, a different error source budget can be accurately represented by R_i^2. ΔF_i contributes over half of this value when $R_i^2 > 0.5$.

Figure 9 shows the R_i^2 of the ring roads' measurements on April 18th and 20th. Interestingly, the sums of the wind speed uncertainty's R^2 and the direction uncertainty's R^2 are all above 0.84, with the highest close to 1, while the other error sources' R^2 values are very low. This could indicate that wind field uncertainty contributed most to the emission flux error in our measurements.

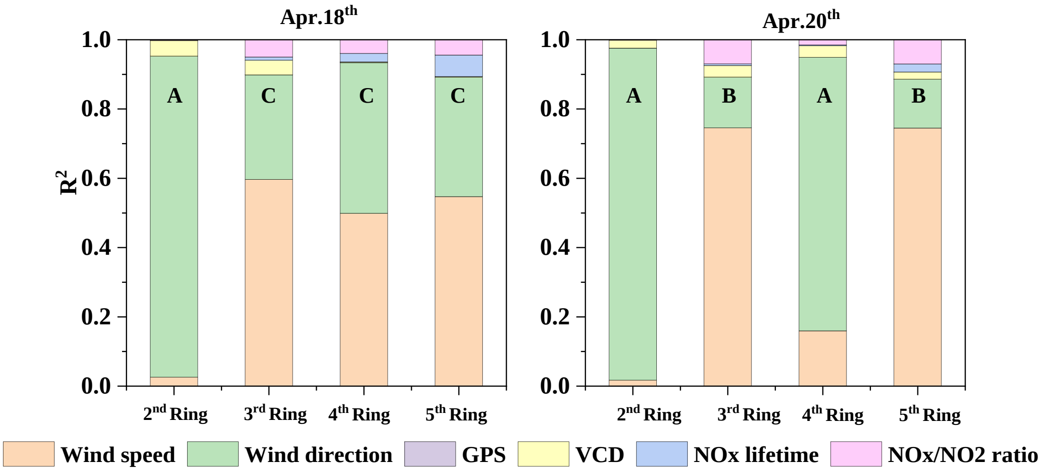

Figure 9. The R_i^2 of the ring roads measured on April 18th and 20th. Group A's main error source is the wind direction uncertainty. Group B's main error source is the wind speed uncertainty. Group C's main error is both the wind direction uncertainty and the wind speed uncertainty.

We also found an extreme case for the second ring on April 18th and extreme cases for the second, third, fourth, and fifth ring on April 20th. The main error source was either wind speed uncertainty or wind direction uncertainty, rather than the common work of wind field uncertainty. This suggests that the main error source of each case may be the sensitivity factors of the emission flux error.

We classified the R^2 values into Groups A, B, and C in Figure 9 to aid the sensitivity study. Groups A, B, and C represented three different cases:

A: the main error source is the wind direction uncertainty;

B: the main error source is the wind speed uncertainty;

C: the error contribution of the wind speed uncertainty and wind direction uncertainty is approximately equal.

4.3.2. Sensitivity to Wind Field Uncertainty

Sensitivity involves studying the relationship between the independent variable change rate (the wind speed uncertainty or the direction's) and the dependent variable change rate (the emission flux error due to wind speed uncertainty or the direction). The independent variable change rates are given by:

$$\Delta\theta = \frac{\theta-\overline{\theta}}{\sigma_\theta}\times 100\%,\ \Delta w = \frac{w-w}{\sigma_w}\times 100\% \tag{17}$$

The dependent variable change rates are given by:

$$r_{\theta|\overline{w}} = \left.\frac{\Delta F_{\theta-\overline{\theta}}}{\Delta F_{NOx}}\right|_{\overline{w}},\ r_{w|\overline{\theta}} = \left.\frac{\Delta F_{w-\overline{w}}}{\Delta F_{NOx}}\right|_{\overline{\theta}} \tag{18}$$

The variations of $r_{\theta|\overline{w}}/r_{w|\overline{\theta}}$ with $\Delta\theta/\Delta w$ are shown in Figure 10. Groups A, B, and C in Figure 10 correspond to the same groups as shown in Figure 9. We also calculated the slope value because of the relationship between $r_{\theta|\overline{w}}/r_{w|\overline{\theta}}$ and $\Delta\theta/\Delta w$, which was linear. This can help assess the sensitivity. The higher the slope, the more sensitive it is to the error source.

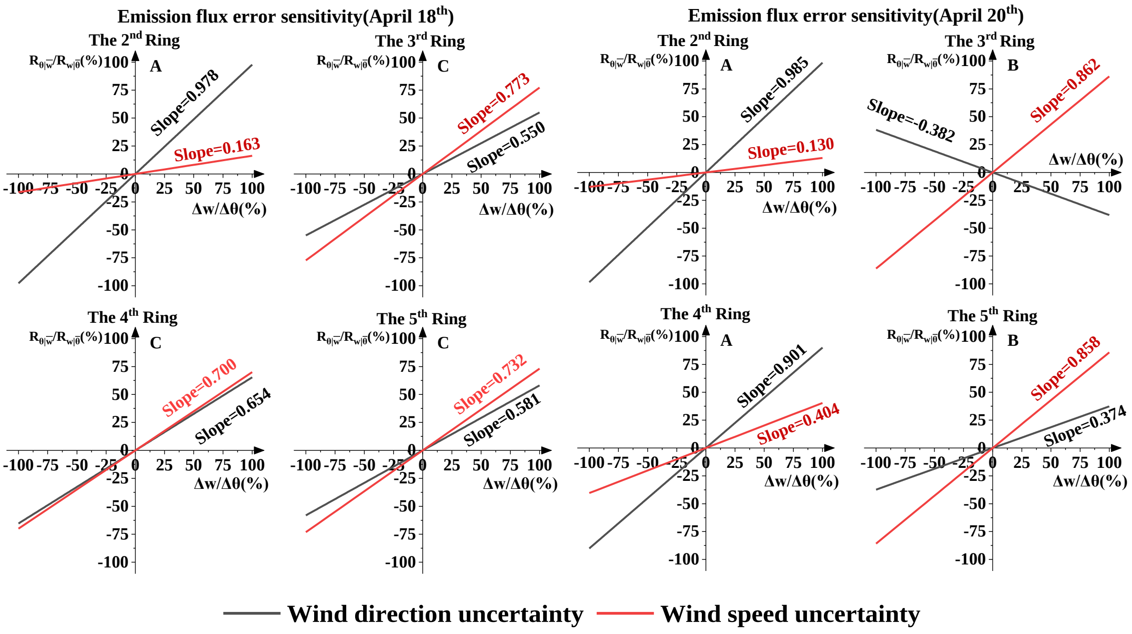

Figure 10. The emission flux error change rate ($r_{\theta|\overline{w}}/r_{w|\overline{\theta}}$) varied with the wind direction/speed change rate ($\Delta\theta/\Delta w$) on April 18th and 20th. The higher the slope, the more sensitive it is to the NO_X emission flux error.

First, we studied the characteristics of Groups A and B. The absolute slope of $r_{\theta|\overline{w}}$ in Group A (varying with $\Delta\theta$) was higher than that of $r_{\theta|\overline{w}}$ while the absolute slope of $r_{w|\overline{\theta}}$ in Group B (varying with Δw) was higher than that of $r_{\theta|\overline{w}}$ A higher slope means a higher growth rate and, in other words, greater sensitivity. Therefore, the emission flux error of Group A was sensitive to wind direction uncertainty and Group B was more sensitive to wind speed uncertainty. Unlike the fifth ring in Group A, the $r_{\theta|\overline{w}}$ slopes of the second ring on April 18th and 20th were much higher than those of $r_{w|\overline{\theta}}$ suggesting that the emission flux error was highly sensitive to wind direction uncertainty.

We made an interesting discovery in Group B (the third ring measurement on April 20th). The $r_{w|\overline{\theta}}$ varied with the Δw, but has a negative trend for $r_{\theta|\overline{w}}$ To explain this, we compared the third ring's VCD with the fifth ring's VCD (see Figure 11). The rectangular as area represented the main high VCD value. The blue arrow was the fifth ring's averaged wind field and the red arrow was the third ring's averaged wind field.

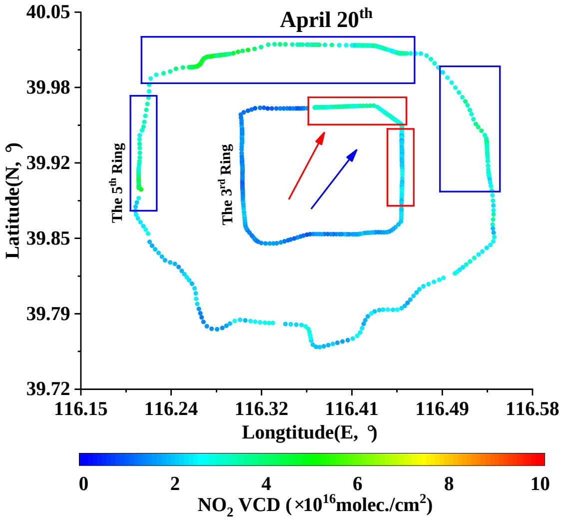

Figure 11. The NO_2 VCD spatial distribution of the fifth ring and third ring on April 20th (The blue arrow is the averaged wind field of the fifth ring. The red arrow is the averaged wind field of the third ring).

The characteristics of the point/industry park source emission measurements by mobile-DOAS suggest that the high VCD value should appear downwind. The high value VCD distribution we measured was approximately vertical to the wind direction. However, the NO_2 VCD for road vehicle exhaust was different. The high value VCD distribution had a relationship with traffic jams and traffic flow, not only with the wind field. The high VCDs in the fifth ring have three distributed sectors, while those in the third ring have two. Clearly, these high VCDs impact the emission flux as the emission flux errors are different. This phenomenon could produce diverse sensitivity to the wind direction and, furthermore, indicates that the NO_X emissions of the road vehicle exhaust measurements are highly sensitive to the wind field. Therefore, more accurate wind field data are necessary.

Second, we studied the characteristics of Group C. Like other groups, the slope in each unit figure of Group C had subtle differences. This indicates that the sensitivity of the emission flux error to the wind speed uncertainty or the directional uncertainty was similar.

Since emission flux error was highly sensitive to wind field uncertainty, the emission flux error may have evident increase if using coarse wind measurements. For coarse wind measurements, wind speed uncertainty, and wind directional uncertainty were roughly estimated as ±1 m/s and ±20°, respectively. The emission flux errors with coarse wind measurements typically increased by about 7%~50%. The wind profile radar used in our experiment was an advantage.

4.3.3. Sensitivity to Other Error Sources

In Section 4.3.2 we determined that the emission flux error was highly sensitive to wind field uncertainty. The sensitivity to other error sources should also be discussed.

We assumed the NO_X atmospheric lifetime uncertainty to be ±1 h. As NO_X decay is a lifetime exponential function, the NO_X emission flux is not very sensitive to NO_X atmospheric lifetime uncertainty. The R_{τ}^{2} is < 0.15, even though the atmospheric lifetime uncertainty is ±2 h. VCD uncertainties are determined by SCD retrieval errors and AMF errors. With the amount of VCD data included in the emission flux calculations, the VCD uncertainties have only a small influence on the emission flux errors. Therefore, for area measurements, emission flux errors are not sensitive to VCD uncertainties.

The NO_X/NO_2 ratio directly acts on NO_X emission flux corrections; thus, NO_X emission flux errors may be sensitive to the uncertainty of this ratio. In Section 4.3.2, we demonstrated what happens when the error source dominates the error budget. For simplicity, we used R^2 to survey the sensitivity, wherein measurements from the fifth ring were tested. The R^2 of the NO_X/NO_2 ratio uncertainty remains above 0.5 when the NO_X/NO_2 ratio uncertainty is >0.4., as shown in Figure 12. This demonstrates that the emission flux error is no longer sensitive to wind field uncertainty when the NO_X/NO_2 ratio uncertainty is > 0.4.

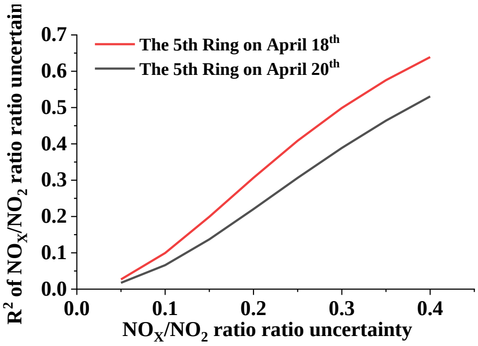

Figure 12. The variation in the R^2 of NO_X/NO_2 ratio uncertainty with NO_X/NO_2 ratio uncertainty.

In the above analysis, we showed the emission flux error budget and the relationship between the emission flux error sensitivity and wind field uncertainty. We found that wind field uncertainty was the main error source for emission flux errors on Beijing's ring roads. For some cases, the NO_X emission flux errors were highly sensitive to wind speed uncertainty or wind direction uncertainty, rather than both. These diverse sensitivities were caused by traffic flow and traffic jam. This study adds to the existing literature on this topic expanding upon the work of previous studies [22–32,34–36]. Our work also indicates that wind information is crucial, as having the actual time and height resolved wind measurements yields great advantages for measuring mega-cities' emission flux.

5. Conclusions

We reported here, for the first time, the use of two mobile-DOAS and a wind profile radar to perform cooperative measurements using data from April 2018.

Two mobile-DOAS systems were used to measure the NO_2 VCD of Beijing's ring road and a wind profile radar was used to measure the near real-time wind field in a short amount of time to determine the NO_X emission flux values of different ring roads. The results show that the NO_X emission flux of Beijing's fifth ring road varied from $(19.29 \pm 5.26) \times 10^{24}$ molec./s to $(36.46 \pm 12.86) \times 10^{24}$ molec./s. Day to day variability in the different ring roads' NO_X emission flux values was also observed in our measurements. At the same time, studying the NO_X emissions from different ring road found that on April 20th, the third ring's NO_X emissions flux was slightly higher than the fourth ring's, because the two ring roads were measured at different time periods. We then performed the emission flux error budget and sensitivity analyses. The main emission flux error source was wind field uncertainty. For some measurements, the main emission flux error source was either wind speed uncertainty or wind direction uncertainty, rather than both. Actual time wind measurements in our experiments decreased the NO_X emission flux error by about 7%~50% compared to coarse wind measurements. The emission flux error sensitivity study indicated that the emission flux error, in some cases, was highly sensitive to wind speed uncertainty or wind direction uncertainty, rather than both. The emission flux error had diverse sensitivity to wind direction uncertainty, which is a novel addition to the existing literature on this topic. This also indicates that wind information is crucial for measuring Beijing's NO_X emission flux values. The NO_X/NO_2 ratio uncertainty sensitivity analyses indicated that the wind field uncertainty no longer dominates the emission flux errors when the NO_X/NO_2 ratio uncertainty is >0.4.

Possessing actual time and height resolved wind measurements and provided a great advantage for NO_X emission flux measurements in Chinese mega-cities. The emission flux errors of different ring roads caused by wind speed uncertainty and wind direction uncertainty were clearly distinguished. Good spatial coverage also provides crucial information for traffic control policies in these cities. Potential advantages of this method are that it can be used to validate the high spatial resolution NOx emission flux derived the TROPOMI [42] and that it can be applied to many other mega-cities in China since most of these cities have a ring road structure, a large scale, and many vehicles.

Author Contributions: Y.H. and A.L. developed the method. Z.H. designed the experiments. Y.H., X.L., and H.R. performed the mobile-DOAS experiment and processed the mobile-DOAS data. X.F. and B.D. helped with the wind measuring. Y.H. and H.R. processed the wind data. P.X., J.X., and X.F. supervised this study. Y.H. analyzed the data and wrote the paper. All authors have read and agreed to the published version of the manuscript.

Funding: This work was supported by National Natural Science Foundation of China (No.:41775029, 91644110, 41530644 and 41975037), National Key Research and Development Project of China (No.: 2018YFC0213201 and 2017YFC0209902), Science and Technology Commission of Shanghai Municipality (No.: 17DZ1203102).

Conflicts of Interest: The authors declare no conflict of interest.

References

1. Seinfeld, J.H.; Pandis, S.N. *Atmospheric Chemistry and Physics: From Air Pollution to Climate Change*; Wiley: Hoboken, NJ, USA, 2016.
2. Cheng, L.X.; Tao, J.H.; Valks, P.; Yu, C.; Liu, S.; Wang, Y.; Xiong, X.Z.; Wang, Z.F.; Chen, L.F. NO_2 Retrieval from the Environmental Trace Gases Monitoring Instrument (EMI): Preliminary Results and Intercomparison with OMI and TROPOMI. *Remote Sens.* **2019**, *11*, 3017. [CrossRef]
3. Mak, H.W.L.; Laughner, J.L.; Fung, J.C.H.; Zhu, Q.; Cohen, R.C. Improved Satellite Retrieval of Tropospheric NO_2 Column Density via Updating of Air Mass Factor (AMF): Case Study of Southern China. *Remote Sens.* **2018**, *10*, 1789. [CrossRef]
4. Squires, F.A.; Nemitz, E.; Langford, B.; Wild, O.; Drysdale, W.S.; Acton, W.J.F.; Fu, P.; Grimmond, C.S.B.; Hamilton, J.F.; Hewitt, C.N.; et al. Measurements of traffic dominated pollutant emissions in a Chinese megacity. *Atmos. Chem. Phys.* **2020**, *20*, 8737–8761. [CrossRef]
5. Wang, Y.; Tao, J.; Cheng, L.; Yu, C.; Wang, Z.; Chen, L. A Retrieval of Glyoxal from OMI over China: Investigation of the Effects of Tropospheric NO_2. *Remote Sens.* **2019**, *11*, 137. [CrossRef]
6. Wen, L.; Xue, L.; Wang, X.; Xu, C.; Chen, T.; Yang, L.; Wang, T.; Zhang, Q.; Wang, W. Summertime fine particulate nitrate pollution in the North China Plain: Increasing trends, formation mechanisms and implications for control policy. *Atmos. Chem. Phys.* **2018**, *18*, 11261–11275. [CrossRef]
7. Zhang, H.X.; Liu, C.; Chan, K.L.; Hu, Q.H.; Liu, H.R.; Li, B.; Xing, C.Z.; Tan, W.; Zhou, H.J.; Si, F.Q.; et al. First observation of tropospheric nitrogen dioxide from the Environ-mental Trace Gases Monitoring Instrument onboard the GaoFen-5 satellite. *Light Sci. Appl.* **2020**, *9*, 66. [CrossRef] [PubMed]
8. Zhang, Q.J.; Beekmann, M.; Freney, E.; Sellegri, K.; Pichon, J.M.; Schwarzenboeck, A.; Colomb, A.; Bourrianne, T.; Michoud, V.; Borbon, A. Formation of secondary organic aerosol in the Paris pollution plume and its impact on surrounding regions. *Atmos. Chem. Phys.* **2015**, *15*, 13973–13992.
9. Wang, Y.; Beirle, S.; Lampel, J.; Koukouli, M.; De Smedt, I.; Theys, N.; Li, A.; Wu, D.; Xie, P.; Liu, C.; et al. Validation of OMI, GOME-2A and GOME-2B tropospheric NO_2, SO_2 and HCHO products using MAX-DOAS observations from 2011 to 2014 in Wuxi, China: Investigation of the effects of priori profiles and aerosols on the satellite products. *Atmos. Chem. Phys.* **2017**, *17*, 5007–5033. [CrossRef]
10. Zhang, Q.; Zheng, Y.X.; Tong, D.; Shao, M.; Wang, S.X.; Zhang, Y.H.; Xu, X.D.; Wang, J.N.; He, H.; Liu, W.Q.; et al. Drivers of improved PM2.5air quality in China from 2013 to 2017. *Proc. Natl. Acad. Sci. USA* **2019**, *116*, 24463–24469. [CrossRef]
11. Platt, U. Dry Deposition of SO_2. *Atmos. Environ.* **1978**, *12*, 363–367. [CrossRef]
12. Platt, U.; Stutz, J. *Differential Optical Absorption Spectroscopy, Principles and Applications*; Springer: Berlin/Heidelberg, Germany, 2008.
13. Wagner, T.; Dix, B.; Friedeburg, C.V.; Frieß, U.; Sanghavi, S.; Sinreich, R. MAX-DOAS O4 measurements: A new technique to derive information on atmospheric aerosols—Principles and information content. *J. Geophys. Res.* **2004**, *109*, D22205. [CrossRef]

14. Bortoli, D.; Silva, A.M.; Costa, M.J.; Domingues, A.F.; Giovanelli, G. Monitoring of atmospheric minor compounds at the Evora Station–Portugal. *Int. J. Remote Sens.* **2009**, *30*, 4209–4226. [CrossRef]
15. Premuda, M.; Petritoli, A.; Masieri, S.; Palazzi, E.; Kostadinov, I.; Bortoli, D.; Ravegnani, F.; Giovanelli, G. A study of O_3 and NO_2 vertical structure in a coastal wooded zone near a metropolitan area, by means of DOAS measurements. *Atmos. Environ.* **2013**, *71*, 104–114. [CrossRef]
16. Premuda, M.; Masieri, S.; Bortoli, D.; Kostadinov, I.; Petritoli, A.; Giovanelli, G. Evaluation of vessel emissions in a lagoon area with ground based Multi axis DOAS measurements. *Atmos. Environ.* **2011**, *45*, 5212–5219. [CrossRef]
17. Wagner, T.; Ibrahim, O.; Shaiganfar, R.; Platt, U. Mobile MAX DOAS observations of tropospheric trace gases. *Atmos. Meas. Tech.* **2010**, *3*, 129–140. [CrossRef]
18. Johanssona, M.; Galle, M.; Yu, T.; Tang, L.; Chen, D.L.; Li, H.J.; Li, J.X.; Zhang, Y. Quantification of total emission of air pollutants from Beijing using mobile mini-DOAS. *Atmos. Environ.* **2008**, *42*, 6926–6933. [CrossRef]
19. Oetjen, H.; Baidar, S.; Krotkov, N.A.; Lamsal, L.N.; Lechner, M.; Volkamer, R. Airborne MAX-DOAS measurements over California: Testing the NASA OMI tropospheric NO_2 product. *J. Geophys. Res. Atmos.* **2013**, *118*, 7400–7413. [CrossRef]
20. Wang, P.; Richter, A.; Bruns, M.; Burrows, J.P.; Scheele, R.; Junkermann, W.; Heue, K.-P.; Wagner, T.; Platt, U.; Pundt, I. Airborne multi-axis DOAS measurements of tropospheric SO_2 plumes in the Po-valley, Italy. *Atmos. Chem. Phys.* **2006**, *6*, 329–338. [CrossRef]
21. Wang, R.W.; Xie, P.H.; Xu, J.; Li, A.; Sun, Y.W. Observation of CO_2 Regional Distribution Using an Airborne Infrared Remote Sensing Spectrometer (Air-IRSS) in the North China Plain. *Remote Sens.* **2019**, *11*, 123. [CrossRef]
22. Rivera, C.; Mellqvist, J.; Samuelsson, J.; Lefer, B.; Alvarez, S.; Patel, M.R. Quantification of NO_2 and SO_2 emissions from Houston Ship Channel and Texas City industrial areas during the 2006 Texas Air Quality Study. *J. Geophys. Res.* **2010**, *115*, D08301. [CrossRef]
23. Constantin, D.-E.; Merlaud, A.; van Roozendael, M.; Voiculescu, M.; Fayt, C.; Hendrick, F.; Pinardi, G.; Georgescu, L. Measurements of Tropospheric NO_2 in Romania Using a Zenith-Sky Mobile DOAS System and Comparisons with Satellite Observations. *Sensors* **2013**, *13*, 3922–3940. [CrossRef] [PubMed]
24. Ibrahim, O.; Shaiganfar, R.; Sinreich, R.; Stein, T.; Platt, U.; Wagner, T. Car MAX-DOAS measurements around entire cities: Quantification of NO_X emissions from the cities of Mannheim and Ludwigshafen (Germany). *Atmos. Meas. Tech.* **2010**, *3*, 709–721. [CrossRef]
25. Frins, E.; Bobrowski, N.; Osorio, M.; Casaballe, N.; Belsterli, G.; Wagner, T.; Platt, U. Scanning and mobile multi-axis DOAS measurements of SO_2 and NO_2 emissions from an electric power plant in Montevideo, Uruguay. *Atmos. Environ.* **2014**, *98*, 347–356. [CrossRef]
26. Davis, Z.Y.W.; Baray, S.; McLinden, C.A.; Khanbabakhani, A.; Fujs, W.; Csukat, C.; Debosz, J.; McLaren, R. Estimation of NO_X and SO_2 emissions from Sarnia, Ontario, using a mobile MAX-DOAS (Multi-AXis Differential Optical Absorption Spectroscopy) and a NO_X analyzer. *Atmos. Chem. Phys.* **2019**, *19*, 13871–13889. [CrossRef]
27. Rivera, C.; Sosa, G.; Wöhrnschimmel, H.; de Foy, B.; Johansson, M.; Galle, B. Tula industrial complex (Mexico) emissions of SO_2 and NO_2 during the MCMA 2006 field campaign using a mobile mini-DOAS system. *Atmos. Chem. Phys.* **2009**, *9*, 6351–6361. [CrossRef]
28. Rivera, C.; Barrera, H.; Grutter, M.; Zavala, M.; Galle, B.; Bei, N.F.; Li, G.H.; Molina, L.T. NO_2 fluxes from Tijuana using a mobile mini-DOAS during Cal-Mex 2010. *Atmos. Environ.* **2012**, *70*, 532–539. [CrossRef]
29. Shaiganfar, R.; Beirle, S.; Sharma, M.; Chauhan, A.; Singh, R.P.; Wagner, T. Estimation of NO_X emissions from Delhi using Car MAX-DOAS observations and comparison with OMI satellite data. *Atmos. Chem. Phys.* **2011**, *11*, 10871–10887. [CrossRef]
30. Wang, S.S.; Zhou, B.; Wang, Z.R.; Yang, S.N.; Hao, N.; Valks, P.; Trautmann, T.; Chen, L.M. Remote sensing of NO_2 emission from the central urban area of Shanghai (China) using the mobile DOAS technique. *J. Geophys. Res.* **2012**, *117*, D13305. [CrossRef]
31. Shaiganfar, R.; Beirle, S.; Denier van der Gon, H.; Jonkers, S.; Kuenen, J.; Petetin, H.; Zhang, Q.; Beekmann, M.; Wagner, T. Estimation of the Paris NO_X emissions from mobile MAX-DOAS observations and CHIMERE model simulations during the MEGAPOLI campaign using the closed integral method. *Atmos. Chem. Phys.* **2017**, *17*, 7853–7890. [CrossRef]

32. Tan, W.; Zhao, S.H.; Liu, C.; Chan, K.L.; Xie, Z.Q.; Zhu, Y.; Sub, W.J.; Zhang, C.X.; Liu, H.R.; Xing, C.Z.; et al. Estimation of winter time NO_X emissions in Hefei, a typical inland city of China, using mobile MAX-DOAS observations. *Atmos. Environ.* **2019**, *200*, 228–242. [CrossRef]
33. Danckaert, T.; Fayt, C.; van Roozendael, M.; de Smedt, I.; Letocart, V.; Merlaud, A.; Pinardi, G. QDOAS Software User Manual. 2017. Available online: http://uv-vis.aeronomie.be/software/QDOAS/QDOAS_manual.pdf (accessed on 9 September 2017).
34. Wu, F.C.; Li, A.; Xie, P.H.; Chen, H.; Hu, Z.K.; Zhang, Q.; Liu, J.G.; Liu, W.Q. Emission Flux Measurement Error with a Mobile DOAS System and Application to NO_X Flux Observations. *Sensors* **2017**, *17*, 231. [CrossRef] [PubMed]
35. Wu, F.; Xie, P.; Li, A.; Mou, F.; Chen, H.; Zhu, Y.; Zhu, T.; Liu, J.; Liu, W. Investigations of temporal and spatial distribution of precursors SO2 and NO2 vertical columns in the North China Plain using mobile DOAS. *Atmos. Chem. Phys.* **2018**, *18*, 1535–1554. [CrossRef]
36. Wu, F.C.; Xie, P.H.; Li, A.; Chan, K.L.; Hartl, A.; Wang, Y.; Si, F.Q.; Zeng, Y.; Qin, M.; Xu, J.; et al. Observations of SO_2 and NO_2 by mobile DOAS in the Guangzhou eastern area during the Asian Games 2010. *Atmos. Meas. Tech.* **2010**, *6*, 2277–2292. [CrossRef]
37. Deutschmann, T.; Beirle, S.; Frieß, U.; Grzegorski, M.; Kern, C.; Kritten, L.; Platt, U.; Prados-Roman, C.; Pukite, J.; Wagner, T.; et al. The Monte Carlo atmospheric radiative transfer model McArtim: Introduction and validation of Jacobians and 3-D features. *J. Quant. Spectrosc. Radiat. Transf.* **2011**, *112*, 1119–1137. [CrossRef]
38. Farrugia, P.S.; Micallef, A. Vectorial statistics for the standard deviation of wind direction. *Meteorol. Atmos. Phys.* **2017**, *129*, 495–506. [CrossRef]
39. Bowers, J.A.; Morton, I.D.; Mould, G.I. Mould. Directional statistics of the wind and waves. *Appl. Ocean. Res.* **1999**, *22*, 13–30. [CrossRef]
40. Mardia, K.V.; Peter, E.J. *Directional Statistics*; John Wiley & Sons: Chichester, UK, 1999.
41. Li, A.; Zhang, J.; Xie, P.H.; Hu, Z.K.; Xu, J.; Mou, F.S.; Wu, F.C.; Liu, J.G.; Liu, W.Q. Variation of temporal and spatial patterns of NO_2 in Beijing using OMI and mobile DOAS. *Sci. China Chem.* **2015**, *58*, 1367–1376. [CrossRef]
42. Steffen Beirle, S.; Borger, C.; Dörner, S.; Li, A.; Hu, Z.K.; Liu, F.; Wang, Y.; Wagner, T. Pinpointing nitrogen oxide emissions from space. *Sci. Adv.* **2019**, *5*, eaax9800. [CrossRef]